Multiple-Sliding-Surface Guidance and Control for Terminal Atmospheric Reentry and Precise Landing

Alessandro Vitiello *
Argotec Srl, Turin, 10155, Italy

Edoardo Maria Leonardi † and Mauro Pontani‡
Sapienza Università di Roma, Rome, 00138, Italy

The development of an effective guidance and attitude control architecture for terminal descent and landing represents a crucial issue for the design of reusable vehicles capable of performing a safe atmospheric planetary entry. The sliding mode control represents a nonlinear technique able to generate an effective real-time closed-loop guidance law, even in the presence of challenging contingencies. This work proposes a multiple sliding-surface guidance control law that is able to drive a lifting vehicle toward safe landing conditions, associated with a desired downrange, crossrange, runway heading, and final vertical velocity at touchdown, even starting from challenging initial conditions. The time derivatives of the lift coefficient and the bank angle are used as the control inputs, whereas the sliding surfaces are defined so that these two inputs are involved simultaneously in the lateral and the vertical guidance. The commanded attitude is pursued by the attitude control system, which employs a feedback nonlinear control law that enjoys quasi-global stability properties. Effectiveness and accuracy of the guidance and control strategy at hand are proven numerically by means of a Monte Carlo campaign, in the presence of stochastic wind and large dispersions on the initial conditions.

Nomenclature

θ_G	=	angular position of Greenwich meridian with respect to the ECI frame
φ	=	geographical latitude [deg]
λ_g	=	geographical longitude [deg]
γ_r	=	flight path angle [deg]
ζ_r	=	heading angle [deg]
$\gamma_r^{(G)}$	=	flight path angle with respect to the II1 frame [deg]

*Aerospace Engineer, System Engineering Unit, Via Cervino, 52
(contribution of this author is based on his activity at Sapienza University of Rome, prior to his employment at Argotec)
†PhD student, Department of Astronautical, Electrical, and Energy Engineering, via Salaria 851
‡Associate Professor, Department of Astronautical, Electrical, and Energy Engineering, via Salaria 851

$\zeta_r^{(G)}$ = heading angle with respect to the II1 frame [deg]

$\overrightarrow{\boldsymbol{r}}$ = vehicle position vector [m]

$\overrightarrow{\boldsymbol{v}_a}$ = local velocity of the atmosphere [m/s]

$\overrightarrow{\boldsymbol{v}_{wind}}$ = local wind velocity [m/s]

$\overrightarrow{\boldsymbol{v}_W}$ = vehicle velocity relative to the atmosphere [m/s]

$\overrightarrow{\boldsymbol{v}_I}$ = vehicle inertial velocity [m/s]

$\overrightarrow{\boldsymbol{v}_r}$ = vehicle relative velocity [m/s]

σ = bank angle [deg]

α = angle of attack [deg]

β = sideslip angle [deg]

α_W, β_W = wind angles [deg]

u_R = vertical wind component [m/s]

u_E = eastward wind component [m/s]

u_N = northward wind component [m/s]

u_W = magnitude of the wind velocity [m/s]

θ_W = random wind direction [deg]

$\overrightarrow{\boldsymbol{A}}$ = aerodynamics force [N]

$\overrightarrow{\boldsymbol{L}}$ = lift force [N]

$\overrightarrow{\boldsymbol{D}}$ = drag force [N]

$\overrightarrow{\boldsymbol{Q}}$ = sideslip force [N]

C_L = lift coefficient

C_D = drag coefficient

C_Q = sideslip coefficient

S_{ref} = aerodynamics surface [m^2]

m = mass of the vehicle [Kg]

ρ = atmospheric density [Kg/m^3]

ρ_0 = atmospheric density at sea level [Kg/m^3]

H = scale altitude [m]

R_{eq} = Earth radius at the equator [m]

CM = height of the center of mass with respect to the runway [m]

(x, y, z) = cartesian coordinates in the II1 frame [m]

r_{down} = downrange distance with respect to the landing runway [m]

r_{cross}	=	crossrange distance with respect to the landing runway [m]
$(\tilde{x}, \tilde{y}, \tilde{z})$	=	cartesian coordinates in the AL frame [m]
$\overrightarrow{\boldsymbol{\omega}_e}$	=	Earth rotation velocity [s^{-1}]
μ	=	planetary constant [m^3/s^2]
$\mathbf{J}_C^{(B)}$	=	vehicle inertia matrix [Kg m^2]
q_0	=	quaternion (scalar part)
$\boldsymbol{q}$	=	quaternion (vector part)
$\boldsymbol{\omega}$	=	angular velocity (3x1-vector) [s^{-1}]
$\boldsymbol{T}_c$	=	commanded torque (3x1-vector) [N m]
$\boldsymbol{T}_a$	=	applied torque (3x1-vector) [N m]
$\boldsymbol{M}_c$	=	disturbance torque (3x1-vector) [N m]
(x_r, y_r, z_r)	=	desired final cartesian coordinates in the II1 frame [m]
$\dot{h}_{des}$	=	desired vertical velocity at touchdown [m/s]
ζ_{rwy}	=	desired final heading angle
t_{go}	=	time required to reach the desired landing point [s]
n_1, n_2	=	sliding mode gains
p_1, p_2, k_1, k_2	=	sliding mode parameters
s_1, s_2, s_3	=	sliding surfaces
V	=	Lyapunov function
$\bar{J}$	=	cost function
q_{0C}	=	commanded quaternion (scalar part)
$\boldsymbol{q}_C$	=	commanded quaternion (vector part)
$\boldsymbol{\omega}_C$	=	commanded angular velocity (3x1-vector) [s^{-1}]
$q_0^{(E)}$	=	error quaternion (scalar part)
$\boldsymbol{q}^{(E)}$	=	error quaternion (vector part)
$\boldsymbol{\omega}_E$	=	error angular velocity (3x1-vector) [s^{-1}]
c_1, c_2	=	gains of the feedback control law
ω_n	=	natural frequency [s^{-1}]
ξ	=	damping coefficient
τ	=	time constant of the actuation model [s]
$\mathbf{R}_{II2\rightarrow B}$	=	attitude matrix

I. Introduction

The development of an autonomous descent and landing guidance strategy for unpowered lifting vehicles represents a crucial issue for the design and technological development of reusable launch and reentry vehicles. Extensive research was focused on reentry of blunt vehicles, such as capsules. Planetary entry using lifting spacecraft increases flexibility and controllability, but introduces further complexity due to sensitivity to unpredictable environmental conditions, such as atmospheric density fluctuations and winds. Early studies on lifting reentry trajectories include the seminal publications by Chapman [1], Frostic and Vinh [2, 3] and Broglio [4]. The Space Shuttle guidance during the approach and landing phase relied on precomputed reference trajectories and was able to accommodate small deviations from the nominal conditions [5].

Recently, the interest in guidance and control technologies for atmospheric reentry and landing of winged vehicles has increased as shown by the development of the European Space Rider program [6] as well as the DLR Reusability Flight Experiment (ReFEx) [7] and the Dream Chaser [8]. Moreover, the use of aerodynamic actions to control the vehicle descent in the atmosphere will be crucial for non-winged vehicles with modest lift-to-drag ratio, as in the newly-designed Orion capsule [9]. Mease and Kremer and Mease et al. [10] revisited the Shuttle reentry guidance using nonlinear geometric methods, leading to an alternative and potentially superior feedback control law. Later on, Benito and Mease [11] developed and applied a new controller based on model prediction that was proven to outperform an alternative feedback linearization scheme when lift saturation occurs. Nonlinear predictive control was used by Guo and Wang [12] as well. Most recently, Lu [13] considered a unified guidance methodology based on a predictor-corrector algorithm, for three types of vehicles. While the great majority of the preceding works is focused on the transatmospheric phase of a lifting vehicle and the related challenges, i.e. thermal and dynamical loads, a more limited number of papers addressed the terminal descent and landing arc, which is traveled after the terminal area energy management interface. Kluever [14] developed a guidance scheme for an unpowered vehicle with limited normal acceleration capabilities. Bollino et al. [15] employed a pseudospectral-based algorithm for optimal feedback guidance of reentry spacecraft, in the presence of large uncertainties and disturbances, with the final aim of driving the reusable vehicle toward a specified landing point. Fahroo and Doman [16] used again a pseudospectral method in a mission scenario with actuation failures. Recently, sliding mode control was proposed as an effective approach to drive an unpowered space vehicle toward a specified landing site [17, 18]. This technique represents an effective nonlinear approach that is able to yield real-time feedback guidance laws. In fact, depending on the instantaneous state and the desired final conditions, sliding mode control was already shown to be effective for generating feasible atmospheric paths leading to safe landing in finite time. In particular, Harl and Balakrishnan [18] developed a real time guidance scheme for the terminal descent and landing of a lifting vehicle, without any need of tracking precomputed trajectories. The latter feature represents a doubtless advantage over implicit-type schemes that rely on precomputed descent paths. In fact, several nonnominal flight conditions may occur that can significantly deviate the vehicle from the

desired trajectory, e.g. winds or aerosurface failures. Usefulness of a real-time algorithm capable of generating online trajectories is apparent, for enhancing the effectiveness of the overall guidance system, thus guaranteeing safe landing even in the presence of challenging contingencies.

The work that follows is based on a recent conference paper [19] and it is intended to extend the previous research on multiple-sliding-surface techniques [17, 18], and apply some new developments to three-dimensional atmospheric descent and landing, with special focus on unpowered reentry vehicles. Specifically, this research considers the problem of driving a lifting spacecraft along its descent path, with (i) specified landing point and prescribed final values of (ii) vertical velocity and (iii) heading angle (for correct alignment with the runway). Significant improvements are proposed with respect to the current state of art:

- the atmospheric reentry is simulated in a complete dynamical framework, where spherical coordinates are employed and transport and Coriolis accelerations are taken into account for translational dynamics;
- the attitude control problem for a 6-degree-of-freedom body is addressed so that a unified architecture for guidance and control is developed. This includes the sampling of the aerodynamic angles generated by the guidance algorithm in order to derive the commanded attitude as well as a simplified modeling of the actuation delay;
- large deviations from the nominal conditions are considered, including the presence of winds, atmospheric density uncertainties and wide dispersions on the initial trajectory variables;
- a gain scheduling strategy is employed in order to extend the capabilities of the guidance algorithm.

While Harl and Balakrishnan [18] took into consideration a simplified two-dimensional model, where only the position and vertical velocity requirements are addressed, Liu et al. [17] made a significant step in the application of multiple sliding surface guidance for terminal approach and landing. However, while a three-dimensional framework is employed, the dynamics is still largely simplified, with no mention of wind perturbations and apparent forces. Also, the attitude control problem is not considered and only limited dispersions on the initial conditions are analyzed. Virgili-Llop et al. [20] and Fedele et al. ([21] - [22]) investigated the use of aerodynamic actions to increase the accuracy on the landing point despite the presence of several disturbing effects. However, they did not address the problem of pinpoint landing of a lifting vehicle with a prescribed vertical velocity and heading angle.

The main objective of this work is the development of a real time guidance and control architecture based on multiple sliding surfaces and nonlinear attitude control, and capable of driving an unpowered winged vehicle to safe touchdown, while fulfilling the landing conditions (i)-(iii). To do this, the time derivatives of the lift coefficient and the bank angle are being used as the control inputs, involved simultaneously in the lateral and the vertical guidance. The existence of constraints on the bank angle and the angle of attack is being addressed as well. Monte Carlo simulations are run in the presence of stochastic wind and large dispersion on the initial spacecraft position and velocity, to test the guidance and control technique at hand, in terms of accuracy at touchdown, with reference to the landing conditions (i)-(iii).

II. Reentry dynamics

This section describes the dynamical model of the unpowered reentry vehicle. The lifting spacecraft is modeled as a 6-degree-of-freedom rigid body, with reference area per mass unit S_{ref}/m and inertia matrix $\mathbf{J}_C^{(B)}$ (taken with respect to the mass center and resolved along the body axes).

A. Reference frames

In the following, the notation $\mathbf{R}_j(\vartheta)(j = 1, 2, 3)$ denotes an elementary rotation about axis j by angle ϑ. Several reference frames must be introduced in order to properly describe the flight dynamics of the reentry vehicle.

- The *Earth-Centered frame* (ECI) $(\hat{c}_1, \hat{c}_2, \hat{c}_3)$ is an inertial reference frame whose origin is in the center of the Earth. The unit vector $\hat{c}_3$ lies along the Earth rotational axis, while $\hat{c}_1$ points toward the vernal axis.
- The *Earth-Centered Earth-Fixed frame* (ECEF) $(\hat{\imath}, \hat{\jmath}, \hat{k})$ is rigidly attached to the Earth. Its origin is in the center of the Earth, with $\hat{\imath}$ intersecting the Greenwich reference meridian at all times, while $\hat{k}$ is aligned with the Earth rotational axis. Assuming that the Earth is rotating with a constant rotational velocity $\underrightarrow{\omega_e} = \omega_e \hat{k}$, the angular position of the reference meridian with respect to the ECI frame is given by the Greenwich sidereal time θ_G, given by $\theta_G(t) = \theta_G(t^*) + \omega_e(t - t^*)$ where t^* is a generic time instant. For simplicity, $\theta_G(t^*) = 0$ is assumed. The ECEF-frame is obtained from the ECI-frame through a single rotation,

$$\begin{bmatrix} \hat{\imath} & \hat{\jmath} & \hat{k} \end{bmatrix}^T = \mathbf{R}_3(\theta_G) \begin{bmatrix} \hat{c}_1 & \hat{c}_2 & \hat{c}_3 \end{bmatrix}^T \tag{1}$$

- The *Auxiliary Landing frame* (AL) $(\hat{r}_L, \hat{E}_L, \hat{N}_L)$ is fixed at the landing point and has the unit vector $\hat{r}_L$ directed upward along the vertical direction, while $\hat{E}_L$ and $\hat{N}_L$ point toward the local East and North direction. If φ_{rwy} and λ_{rwy} are the latitude and geographical longitude at the landing point, then

$$\begin{bmatrix} \hat{r}_L & \hat{E}_L & \hat{N}_L \end{bmatrix}^T = \mathbf{R}_2(-\varphi_{rwy})\mathbf{R}_3(\lambda_{rwy}) \begin{bmatrix} \hat{\imath} & \hat{\jmath} & \hat{k} \end{bmatrix}^T \tag{2}$$

- The *Local Horizontal frame* (LH) $(\hat{r}, \hat{E}, \hat{N})$ is a reference system attached to the reentry vehicle. Specifically, $\hat{r}$ is aligned with the instantaneous position vector $\underrightarrow{\boldsymbol{r}}$, $\hat{E}$ is directed along the East direction, and $\hat{N}$ is aligned with the local North direction. This frame is obtained from the ECEF-frame through two elementary rotations: a counterclockwise rotation by angle λ_g about axis 3 and a clockwise rotation by angle φ about axis 2. Therefore

$$\begin{bmatrix} \hat{r} & \hat{E} & \hat{N} \end{bmatrix}^T = \mathbf{R}_2(-\varphi)\mathbf{R}_3(\lambda_g) \begin{bmatrix} \hat{\imath} & \hat{\jmath} & \hat{k} \end{bmatrix}^T \tag{3}$$

- *The Relative Velocity frame* (RV) $(\hat{n}_r, \hat{v}_r, \hat{h}_r)$ is obtained from the LH frame through a counterclockwise rotation about axis 1 by angle ζ_r (heading angle) and a clockwise rotation about axis 3 by angle gamma γ_r (flight path

angle)

$$\begin{bmatrix} \hat{n}_r & \hat{v}_r & \hat{h}_r \end{bmatrix}^T = \mathbf{R}_3(-\gamma_r)\mathbf{R}_1(\zeta_r) \begin{bmatrix} \hat{r} & \hat{E} & \hat{N} \end{bmatrix}^T \tag{4}$$

- The *Wind Axes frame* (WA) $(\hat{n}_W, \hat{v}_W, \hat{h}_W)$ is defined with reference to the vehicle velocity with respect to the local velocity of the atmosphere $\underrightarrow{v_a}$, which is

$$\underrightarrow{v_a} = \underrightarrow{\omega_e} \times \underrightarrow{r} + \underrightarrow{v_{wind}} \tag{5}$$

where $\underrightarrow{v_{wind}}$ corresponds to local wind. The vehicle velocity relative to the atmosphere is thus

$$\underrightarrow{v_W} = \underrightarrow{v_I} - \underrightarrow{v_a} = \underrightarrow{v_I} - (\underrightarrow{\omega_e} \times \underrightarrow{r} + \underrightarrow{v_{wind}}) = \underrightarrow{v_r} - \underrightarrow{v_{wind}} \tag{6}$$

where $\underrightarrow{v_I}$ and $\underrightarrow{v_r}$ are the inertial and relative velocity respectively. Unit vector $\hat{v}_W$ is aligned with the velocity vector $\underrightarrow{v_W}$. This vector is defined in the RV frame through a counterclockwise rotation about axis 1 by angle α_W followed by a second clockwise rotation about axis 3 by angle β_W. Then, the unit vector $\hat{n}_W$ is contained in the plane of symmetry of the vehicle and is directed upward in the presence of horizontal flight conditions. Thus, the WA frame is obtained from the RV frame through the following rotations

$$\begin{bmatrix} \hat{n}_W & \hat{v}_W & \hat{h}_W \end{bmatrix}^T = \mathbf{R}_2(\sigma)\mathbf{R}_3(-\beta_W)\mathbf{R}_1(\alpha_W) \begin{bmatrix} \hat{n}_r & \hat{v}_r & \hat{h}_r \end{bmatrix}^T \tag{7}$$

- The *Auxiliary Body Axes frame* (ABA) $(\hat{i}_B, \hat{j}_B, \hat{k}_B)$ is aligned with the vehicle body axes. The unit vector $\hat{k}_B$ is orthogonal to the vehicle plane of symmetry, while the two remaining unit vectors lie on it. The ABA frame is obtained from the WA frame through a counterclockwise rotation about axis 1 by angle β (sideslip angle) and a clockwise rotation about axis 3 by angle α (angle of attack).

$$\begin{bmatrix} \hat{i}_B & \hat{j}_B & \hat{k}_B \end{bmatrix}^T = \mathbf{R}_3(-\alpha)\mathbf{R}_1(\beta) \begin{bmatrix} \hat{n}_W & \hat{v}_W & \hat{h}_W \end{bmatrix}^T \tag{8}$$

- The *Body Axes frame* (BA) $(\hat{x}_B, \hat{y}_B, \hat{z}_B)$ has axis $\hat{x}_B$ aligned with the longitudinal axis and the unit vector $\hat{z}_B$ directed downward (in horizontal flight conditions). Thus

$$\begin{bmatrix} \hat{x}_B & \hat{y}_B & \hat{z}_B \end{bmatrix}^T = \begin{bmatrix} 0 & 1 & 0 \\ 0 & 0 & -1 \\ -1 & 0 & 0 \end{bmatrix} \begin{bmatrix} \hat{i}_B & \hat{j}_B & \hat{k}_B \end{bmatrix}^T = \mathbf{R}_A \begin{bmatrix} \hat{i}_B & \hat{j}_B & \hat{k}_B \end{bmatrix}^T \tag{9}$$

- The *Iterative Inertial frame 1* (II1) $(\hat{r}_k, \hat{E}_k, \hat{N}_k)$ is defined with the absolute longitude and latitude (λ_k, φ_k) at the beginning of each sampling time interval and has axes aligned with those of the LH-frame at each sampling time.

$$\left[\hat{r}_k, \hat{E}_k, \hat{N}_k\right]^T = \mathbf{R}_2(-\varphi_k)\mathbf{R}_3(\lambda_k)\left[\hat{c}_1 \quad \hat{c}_2 \quad \hat{c}_3\right]^T \tag{10}$$

- The *Iterative Inertial frame 2* (II2) $(\hat{i}_k, \hat{j}_k, \hat{k}_k)$ is obtained from II1 through

$$\left[\hat{i}_k \quad \hat{j}_k \quad \hat{k}_k\right]^T = \begin{bmatrix} 0 & 0 & 1 \\ 0 & 1 & 0 \\ -1 & 0 & 0 \end{bmatrix}\left[\hat{r}_k \quad \hat{E}_k \quad \hat{N}_k\right]^T = \mathbf{R}_B\left[\hat{r}_k \quad \hat{E}_k \quad \hat{N}_k\right]^T \tag{11}$$

Figure 1 shows the different reference frames and the related rotation matrices.

B. Wind modeling

The wind velocity is specified in terms of its components in the LH frame

$$\begin{aligned} u_R &= 0 \\ u_E &= u_W \cos(\theta_W) \\ u_N &= u_W \sin(\theta_W) \end{aligned} \tag{12}$$

where θ_W is the random wind direction (with uniform distribution in [0,2π]), assumed constant with respect to the altitude in each simulation, and u_W is the magnitude of the wind. This is given by the following mean wind profile as a function of the altitude x [23]:

$$u_W = u_{xy}\frac{\ln\left(\frac{x}{z_0}\right)}{\ln(133.4)} \tag{13}$$

where z_0 is a constant equal to 0.0457 m for terminal flight phases, while u_{xy} is the wind speed at an altitude of 6.096 m, which is randomly generated according to a Gaussian distribution. Then, the wind components must be projected along the RV frame

$$\boldsymbol{v}_{wind} = \mathbf{R}_1^T(\zeta_r)\mathbf{R}_3^T(-\gamma_r)\left[u_R \quad u_E \quad u_N\right]^T \tag{14}$$

Therefore, in the RV frame the vehicle velocity relative to the atmosphere is

$$\boldsymbol{v}_W = \left[-v_{wind,1} \quad v_r - v_{wind,2} \quad -v_{wind,3}\right]^T \tag{15}$$

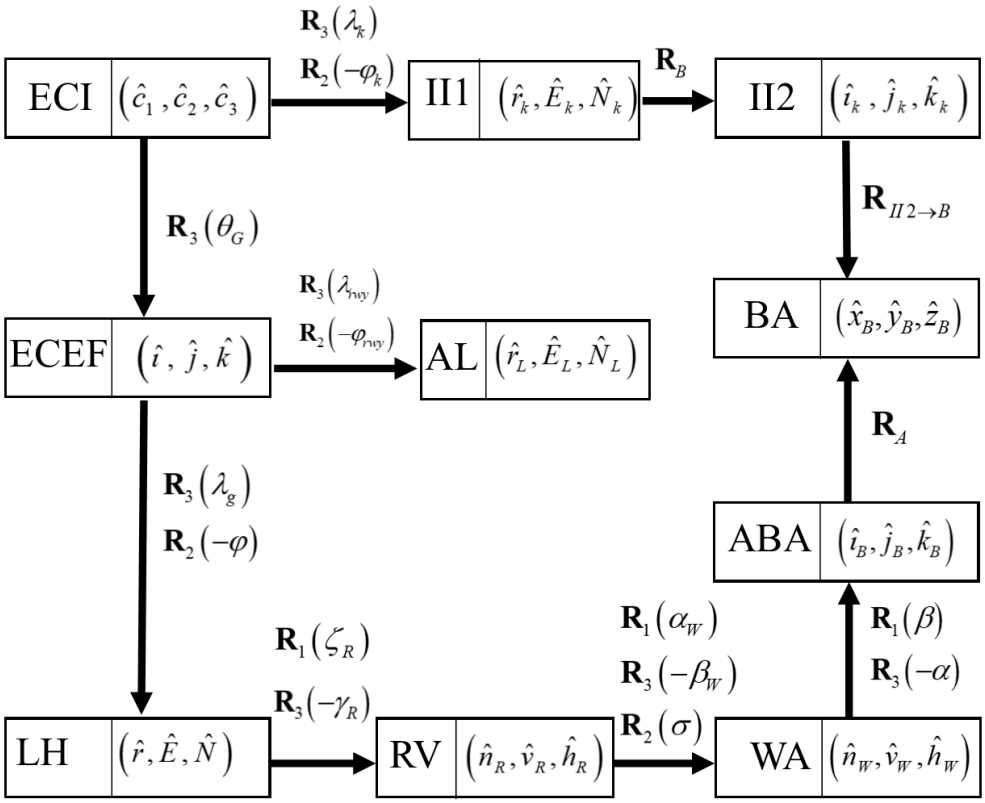

- **ECI** : Earth Center Inertial
- **ECEF** : Earth-Centered Earth-Fixed
- **AL** : Auxiliary Landing
- **LH** : Local Horizontal
- **RV** : Relative Velocity
- **WA** : Wind Axes
- **ABA** : Auxiliary Body Axes
- **BA** : Body Axes
- **II1** : Iterative Inertial 1
- **II2** : Iterative Inertial 2

Fig. 1 Reference frames and related rotation matrices

Finally, the two angles α_W and β_W can be obtained as

$$\beta_W = \arcsin \frac{-v_{w,3}}{v_W} \tag{16}$$

$$\begin{cases} \sin \alpha_W = \dfrac{-v_{w,1}}{v_W \cos \beta_W} \\ \cos \alpha_W = \dfrac{v_r - v_{w,2}}{v_W \cos \beta_W} \end{cases} \tag{17}$$

C. Aerodynamics modeling

The forces acting on the vehicle are the gravity force and the aerodynamic force $\underset{\rightarrow}{\boldsymbol{A}}$. The components of the aerodynamic force can be conveniently expressed in the WA frame. These are given by the lift $\underset{\rightarrow}{\boldsymbol{L}}$, the drag $\underset{\rightarrow}{\boldsymbol{D}}$, and the side force $\underset{\rightarrow}{\boldsymbol{Q}}$:

$$\underset{\rightarrow}{\boldsymbol{A}} = \underset{\rightarrow}{\boldsymbol{L}} + \underset{\rightarrow}{\boldsymbol{D}} + \underset{\rightarrow}{\boldsymbol{Q}} \tag{18}$$

Therefore, the expressions for the forces are given by

$$\underset{\rightarrow}{\boldsymbol{L}} = \tilde{L}\hat{n}_W = \frac{1}{2}C_L(\alpha)S_{ref}\rho v_W^2\hat{n}_W \tag{19}$$

$$\underset{\rightarrow}{\boldsymbol{D}} = -\tilde{D}\hat{v}_W = -\frac{1}{2}C_D(\alpha)S_{ref}\rho v_W^2\hat{v}_W \tag{20}$$

$$\underset{\rightarrow}{\boldsymbol{Q}} = \tilde{Q}\hat{h}_W = \frac{1}{2}C_Q(\beta)S_{ref}\rho v_W^2\hat{h}_W \tag{21}$$

where ρ is the local atmospheric density. The symbols C_L , C_D and C_Q denote the lift, drag and the side force coefficients, which are assumed to depend only on the angle of attack [18] and the sideslip angle, as follows

$$C_L(\alpha) = C_{L0}\sin^2\alpha\cos\alpha \tag{22}$$

$$C_D(\alpha) = C_{D0} + KC_L^2 \tag{23}$$

$$C_Q(\beta) = C_{Q0}\sin^2\beta\cos\beta \tag{24}$$

where $C_{L0} = 2.3$, $C_{D0} = 0.0975$, $C_{Q0} = 0.5C_{L0}$ and $K = 0.1819$ [18]. The value of C_{Q0} was assumed on the basis of the data contained in [24] for similar lifting vehicles. Then, the aerodynamic forces must be projected onto the RV frame through the angles α_W, β_W and σ. The acceleration components are denoted with $(A_n, A_v, A_h,)$ and given by

$$\underset{\rightarrow}{\boldsymbol{A}} = \begin{bmatrix} A_n & A_v & A_h \end{bmatrix}\begin{bmatrix} \hat{n}_r & \hat{v}_r & \hat{h}_r \end{bmatrix}^T = \begin{bmatrix} \frac{\tilde{L}}{m} & -\frac{\tilde{D}}{m} & \frac{\tilde{Q}}{m} \end{bmatrix}\mathbf{R}_2(\sigma)\mathbf{R}_3(-\beta_W)\mathbf{R}_1(\alpha_W)\begin{bmatrix} \hat{n}_r & \hat{v}_r & \hat{h}_r \end{bmatrix}^T \tag{25}$$

Atmospheric density is modeled using the exponential function

$$\rho = \rho_0\exp\left(-z/H\right) \tag{26}$$

where ρ_0 = 1.225 Kg/m^3 is the density at sea level and H = 8500 m is the scale height [18].

D. Trajectory

The unpowered lifting vehicle is modeled as a 6-degrees-of-freedom (6-DOF) rigid body. The position of the center of mass of the vehicle is identified by the three spherical coordinates (r, λ_g, φ). The other three state variables are the relative velocity magnitude v_r, the heading angle ζ_r, and the flight path angle γ_r. The equations of motion are written under the assumption that the vehicle is unpowered [3],

$$\dot{r} = v_r \sin\gamma_r \tag{27}$$

$$\dot{\lambda}_g = \frac{v_r \cos\gamma_r \cos\zeta_r}{r\cos\varphi} \tag{28}$$

$$\dot{\varphi} = \frac{v_r \cos\gamma_r \sin\zeta_r}{r} \tag{29}$$

$$\dot{v}_r = -\frac{\mu}{r^2}\sin\gamma_r + A_v + \omega_e^2 r\cos\varphi(\cos\varphi\sin\gamma_r - \sin\varphi\cos\gamma_r\sin\zeta_r) \tag{30}$$

$$\dot{\zeta}_r = -\frac{v_r}{r}\tan\varphi\cos\gamma_r\cos\zeta_r + \frac{A_h}{v_r\cos\gamma_r} + 2\omega_e\cos\varphi\tan\gamma_r\sin\zeta_r - \frac{\omega_e^2 r}{v_r\cos\gamma_r}\sin\varphi\cos\varphi\cos\zeta_r - 2\omega_e\sin\varphi \tag{31}$$

$$\dot{\gamma}_r = \left[-\frac{\mu}{r^2 v_r}\right]\cos\gamma_r + \frac{A_n}{v_r} + 2\omega_e\cos\varphi\cos\zeta_r + \frac{\omega_e^2 r}{v_r}\cos\varphi(\cos\varphi\cos\gamma_r + \sin\varphi\sin\gamma_r\sin\zeta_r) \tag{32}$$

where ω_e and μ are the Earth rotational rate and gravitational parameter. A_r, A_n and A_h include the reference area per mass unit S_{ref}/m, which equals 0.005804 m^2/Kg [18], which is a value typical of a winged vehicle.

E. Attitude

The attitude dynamics equations are given by [25]

$$\mathbf{J}_C^{(B)}\dot{\boldsymbol{\omega}} = -\tilde{\boldsymbol{\omega}}\mathbf{J}_C^{(B)}\boldsymbol{\omega} + \boldsymbol{T}_a + \boldsymbol{M}_c \tag{33}$$

where $\mathbf{J}_C^{(B)}$ is the vehicle inertia matrix with respect to the center of mass, $\boldsymbol{\omega}$ is the (3x1) vector that includes the components along the body axes of the vehicle angular velocity with respect to the inertial frame II2, $\boldsymbol{T}_a$ is the (3×1)

vector that includes the components along the body axes of the actual control torque, $\boldsymbol{M}_c$ is the (3×1) vector that includes the components of the disturbing torque along the body axes, while $\tilde{\boldsymbol{\omega}}$ is the the skew-symmetric matrix associated with $\boldsymbol{\omega}$. The kinematics equations have the following compact form [25]:

$$\dot{q}_0 = -\frac{1}{2}\boldsymbol{\omega}^T \, \boldsymbol{q} \tag{34}$$

$$\dot{\boldsymbol{q}} = -\frac{1}{2}\tilde{\boldsymbol{\omega}} \, \boldsymbol{q} + \frac{1}{2} q_0 \boldsymbol{\omega} \tag{35}$$

where $(q_0, \boldsymbol{q})$ are the Euler parameters (quaternions). In this work, the inertia matrix is assumed to be [26]

$$\mathbf{J}_C^{(B)} = 1.0e+06 \begin{bmatrix} 0.5888 & 0 & -0.0242 \\ 0 & 1.3032 & 0 \\ -0.0242 & 0 & 1.5342 \end{bmatrix} \quad \text{Kg m}^2 \tag{36}$$

III. Multiple-sliding surface guidance

This section considers the application of multiple-sliding-surface guidance to terminal descent and landing. For the definition of the sliding surfaces, the equations of motion will be used under the hypotheses that (i) the gravitational field is uniform and (ii) the apparent forces (terms depending on ω_e) are negligible, as well as (iii) the term v_r/r in the equation for $\dot{\zeta}_r$ (compared to the term with A_h). Thus, the equations of motion are simplified to

$$\dot{x} = v_r^{(G)} \sin \gamma_r^{(G)} \tag{37}$$

$$\dot{y} = v_r^{(G)} \cos \gamma_r^{(G)} \cos \zeta_r^{(G)} \tag{38}$$

$$\dot{z} = v_r^{(G)} \cos \gamma_r^{(G)} \sin \zeta_r^{(G)} \tag{39}$$

$$\dot{v}_r^{(G)} = -g \sin \gamma_r^{(G)} + A_v \tag{40}$$

$$\dot{\zeta}_r^{(G)} = \frac{A_h}{v_r^{(G)} \cos \gamma_r^{(G)}} \tag{41}$$

$$\dot{\gamma}_r^{(G)} = \frac{g\cos\gamma_r^{(G)}}{v_r^{(G)}} + \frac{A_n}{v_r^{(G)}} \tag{42}$$

where $\gamma_r^{(G)}$ and $\zeta_r^{(G)}$ are the flight path angle and the heading angle with respect to the II1 frame, and (x, y, z) are the cartesian coordinates in the II1 frame:

$$\begin{bmatrix} x \\ y \\ z \end{bmatrix}^T = \begin{bmatrix} r\cos\varphi\cos\lambda_g \\ r\cos\varphi\sin\lambda_g \\ r\sin\varphi \end{bmatrix}^T \mathbf{R}_3(\theta_G)\mathbf{R}_3^T(\lambda_k)\mathbf{R}_2^T(-\varphi_k) - \begin{bmatrix} R_{eq} \\ 0 \\ 0 \end{bmatrix}^T \tag{43}$$

A. Flight conditions at touchdown

The goal of the guidance algorithm is in successfully driving the vehicle toward a safe touchdown at the desired landing point, with specified heading angle and vertical velocity. The coordinates of the landing site (x_r, y_r, z_r) are defined in the II1 frame

$$\begin{bmatrix} x_r \\ y_r \\ z_r \end{bmatrix}^T = (R_{eq} + CM) \begin{bmatrix} \cos\varphi_{rwy}\cos\lambda_{rwy} \\ \cos\varphi_{rwy}\sin\lambda_{rwy} \\ \sin\varphi_{rwy} \end{bmatrix}^T \mathbf{R}_3(\theta_G)\mathbf{R}_3^T(\lambda_k)\mathbf{R}_2^T(-\varphi_k) - \begin{bmatrix} R_{eq} \\ 0 \\ 0 \end{bmatrix}^T \tag{44}$$

In Eq. (44) the expected height on the center of mass with respect to the runway is reported ($CM = 3$ m). Moreover, the vehicle must land with the desired vertical speed and with the proper alignment with the runway

$$\begin{aligned} \dot{x}(t_r) &= \dot{h}_{des} \\ \zeta(t_r) &= \zeta_{rwy} \end{aligned} \tag{45}$$

where $\dot{h}_{des}$ is set to -1.5 m/s and ζ_{rwy} is the heading angle of the NASA Space Shuttle Landing Facility (with respect to the East direction), equal to -60.24 deg.

B. Guidance strategy

The desired landing conditions can be written in terms of a 2-dimensional sliding surface $\boldsymbol{s}_1$, that the guidance algorithm must drive to zero in a finite time t_r,

$$\boldsymbol{s}_1 = \begin{bmatrix} x - x_r + \dot{h}_{des} t_{go} \\ y - x\tan\zeta_{rwy} - (y_r - x_r\tan\zeta_{rwy}) \end{bmatrix} \tag{46}$$

where t_{go} is the approximation of the time required to reach the desired landing point

$$t_{go} = \frac{\sqrt{(x_r - x)^2 + (y_r - y)^2 + (z_r - z)^2}}{v_r} = t_r - t \tag{47}$$

The first component of $\boldsymbol{s}_1$ is responsible for the vertical guidance, while the second component guarantees the correct alignment with the runway. Equation (47) shows that, if the algorithm is capable of driving the sliding surfaces to zero, then

$$x \to x_r, \;\; y \to y_r, \;\; z \to z_r, \;\; \text{as} \;\; t_{go} \to 0 \tag{48}$$

The sliding surfaces are differentiated until the control variables $\dot{C}_L$ and σ appear in an affine form

$$\dot{\boldsymbol{s}}_1 = \begin{bmatrix} \dot{x} - \dot{h}_{des} \\ \dot{y} - \dot{z}\tan\zeta_{rwy} \end{bmatrix} = \begin{bmatrix} v_r^{(G)}\sin\gamma_r^{(G)} - \dot{h}_{des} \\ v_r^{(G)}\cos\gamma_r^{(G)}\cos\zeta_r^{(G)} - v_r^{(G)}\cos\gamma_r^{(G)}\sin\zeta_r^{(G)}\tan\zeta_{rwy} \end{bmatrix} \tag{49}$$

$$\ddot{\boldsymbol{s}}_1 = \begin{bmatrix} a_1 \\ a_2 \end{bmatrix} = \boldsymbol{a} \tag{50}$$

$$\dddot{\boldsymbol{s}}_1 = \begin{bmatrix} b_1 + c_{11}\dot{C}_L + c_{12}\dot{\sigma} \\ b_2 + c_{21}\dot{C}_L + c_{22}\dot{\sigma} \end{bmatrix} = \boldsymbol{b} + \mathbf{C}\,\boldsymbol{u} \tag{51}$$

The full expression of the coefficients depends only on the state variables and is reported in the Appendix. From Eq. (49), it is clear that the vehicle reaches the landing point with the desired vertical velocity $\dot{h}_{des}$ and the desired heading angle ζ_{rwy}, when the surface $\boldsymbol{s}_1$ and its derivatives $\dot{\boldsymbol{s}}_1, \ddot{\boldsymbol{s}}_1$ are both driven to zero. Instead, Eq. (51) shows that the control inputs appear in the third derivative of the sliding surface. Thus, a higher-order sliding mode approach is used, meaning that both the sliding surface and its first and second derivatives are driven to zero,

$$\boldsymbol{s}_1 = \dot{\boldsymbol{s}}_1 = \ddot{\boldsymbol{s}}_1 = 0 \tag{52}$$

Then, the control variables must be defined so that the sliding surface and its second and third derivatives tend to zero. With this aim, the derivatives of the sliding surfaces are taken as virtual control inputs. A candidate Lyapunov function is thus defined as

$$V_1 = \frac{1}{2}\boldsymbol{s}_1^T\boldsymbol{s}_1 \tag{53}$$

$$\dot{V}_1 = \boldsymbol{s}_1^T \dot{\boldsymbol{s}}_1 \tag{54}$$

Of course, $\dot{V}_1$ must be negative-definite. To do this, $\dot{\boldsymbol{s}}_1$ is chosen as

$$\dot{\boldsymbol{s}}_1 = -\boldsymbol{\Gamma}\frac{\boldsymbol{s}_1}{t_r - t} = -\boldsymbol{\Gamma}\frac{\boldsymbol{s}_1}{t_{go}} \tag{55}$$

This guarantees that the sliding surface tends to zero in a finite time t_r , provided that

$$\boldsymbol{\Gamma} = \begin{bmatrix} n_1 & 0 \\ 0 & n_2 \end{bmatrix} \qquad n_1,\ n_2 > 1 \tag{56}$$

It is remarkable that the expression for $\dot{\boldsymbol{s}}_1$ is an adaptive term, which changes in relation to the trajectory the sliding surface is following. The condition in Eq. (55) can be considered as a new sliding surface, defined as

$$\boldsymbol{s}_2 = \dot{\boldsymbol{s}}_1 + \frac{\boldsymbol{\Gamma}\boldsymbol{s}_1}{t_r - t} \tag{57}$$

This surface is differentiated again, to yield

$$\dot{\boldsymbol{s}}_2 = \boldsymbol{a} + \frac{\boldsymbol{\Gamma}\dot{\boldsymbol{s}}_1 t_{go} + \boldsymbol{\Gamma}\boldsymbol{s}_1}{t_{go}^2} \tag{58}$$

Finally, the last sliding surface is defined as

$$\boldsymbol{s}_3 = \dot{\boldsymbol{s}}_2 + \frac{\boldsymbol{\Gamma}\boldsymbol{s}_2}{t_{go}} \tag{59}$$

The time derivative of $\boldsymbol{s}_3$ is

$$\dot{\boldsymbol{s}}_3 = \boldsymbol{b} + \mathbf{C}\,\boldsymbol{u} + \frac{\boldsymbol{\Gamma}\boldsymbol{a}t_{go}^2 + 2(\boldsymbol{\Gamma}\dot{\boldsymbol{s}}_1 t_{go} + \boldsymbol{\Gamma}\boldsymbol{s}_1)}{t_{go}^3} + \frac{\boldsymbol{\Gamma}\dot{\boldsymbol{s}}_2 t_{go} + \boldsymbol{\Gamma}\boldsymbol{s}_1}{t_{go}^2} \tag{60}$$

where $t - t_r = t_{go}$ as in Eq. (47). The goal of the control input is to force the derivative to satisfy Eq. (55). In order to guarantee the convergence of both the sliding surface and its derivatives, it is important that the condition in Eq. (55) is reached in a finite time t_r^* before the reaching time t_r [18]. Therefore, a necessary condition for convergence is that

$$t_r^* < t_r \tag{61}$$

Again, a Lyapunov function can be defined as

$$V_3 = \frac{1}{2}\boldsymbol{s}_3^T \boldsymbol{s}_3 \tag{62}$$

Therefore,

$$\dot{V}_3 = \boldsymbol{s}_3^T \dot{\boldsymbol{s}}_3 \tag{63}$$

The control is thus selected as

$$\boldsymbol{u} = -\mathbf{C}^{-1}\left[\boldsymbol{b} + \frac{\boldsymbol{\Gamma a} t_{go}^2 + 2(\boldsymbol{\Gamma}\dot{\boldsymbol{s}}_1 t_{go} + \boldsymbol{\Gamma s}_1)}{t_{go}^3} + \frac{\boldsymbol{\Gamma}\dot{\boldsymbol{s}}_2 t_{go} + \boldsymbol{\Gamma s}_1}{t_{go}^2} + \boldsymbol{\Lambda} sgn(\boldsymbol{s}_3)\right] \tag{64}$$

with

$$\boldsymbol{\Lambda} = \begin{bmatrix} \frac{|\boldsymbol{s}_{3,1}(0)|}{t_{r1}^*} & 0 \\ 0 & \frac{|\boldsymbol{s}_{3,2}(0)|}{t_{r2}^*} \end{bmatrix} \tag{65}$$

The terms $\boldsymbol{s}_{3,1}(0)$ and $\boldsymbol{s}_{3,2}(0)$ are components 1 and 2 of $\boldsymbol{s}_3$ at the initial time, while $t_{r1}^* = p_1 t_r$ and $t_{r2}^* = p_2 t_r$, with $p_1, p_2 < 1$ and denoting two dimensionless parameters to tune. The selection of these parameters is based on an adaptive strategy,

$$p_1 = k_1 \frac{|\boldsymbol{\Lambda}_{11}^0|}{\boldsymbol{s}_{3,1}} \tag{66}$$

$$p_2 = k_2 \frac{|\boldsymbol{\Lambda}_{22}^0|}{\boldsymbol{s}_{3,2}} \tag{67}$$

with $k_1 = k_2 = 10^{0.45}$, while $\boldsymbol{\Lambda}_{11}^0$ and $\boldsymbol{\Lambda}_{22}^0$ are the two diagonal terms of

$$\boldsymbol{\Lambda}^0 = \begin{bmatrix} \frac{|\boldsymbol{s}_{3,1}(0)|}{t_r} & 0 \\ 0 & \frac{|\boldsymbol{s}_{3,2}(0)|}{t_r} \end{bmatrix} \tag{68}$$

This allows tuning the control effort according to the instantaneous value of the sliding surface. Matrix $\boldsymbol{\Lambda}$ allows establishing how quickly the sliding surface $\boldsymbol{s}_3$ decreases to zero. Moreover, the reaching time t_r must be updated at each iteration,

$$t_r = t + t_{go} \tag{69}$$

where t_{go} is evaluated taking into consideration the instantaneous range and velocity as in Eq. (44).

Finally, the commanded control inputs are saturated among reasonable values in order to generate only feasible trajectories

$$0 \ \text{deg} \leq \alpha_c \leq 40 \ \text{deg} \quad , \quad -50 \ \text{deg} \leq \sigma_c \leq 50 \ \text{deg} \tag{70}$$

Moreover, the following constraints are considered:

$$|\omega_i^{(G)}| \leq 40 \ \text{deg/s} \quad , \quad |\dot{\omega}_i^{(G)}| \leq 5 \ \text{deg/s}^2 \quad (i = 1, 2, 3) \tag{71}$$

where subscript i denotes component i of the respective vector and superscript G refers to the commanded value generated by the guidance algorithm. Finally, in order to provide a smooth flare, the following constraints are added while flying below 5 m

$$\begin{gathered} \sigma = 0 \ \text{deg} \\ |\omega_i^{(G)}| = 0 \ \ \text{deg/s} \ \ (i = 1, 3) \ , \quad |\omega_2^{(G)}| \leq 3 \ \ \text{deg/s} \\ |\dot{\omega}_i^{(G)}| \leq 1 \ \ \text{deg/s}^2 \ \ (i = 1, 2, 3) \end{gathered} \tag{72}$$

C. Optimal gain selection

The guidance scheme requires a careful selection of the two parameters n_1, n_2, which strongly influence the outcome of the trajectory generation. The gains are selected in order to guarantee the closest distance from the landing point and a modest value of the final lift coefficient (C_{Lf}) and bank angle (σ_f). Therefore, an optimization procedure was set, in order to minimize the following cost function:

$$\bar{J} = \sqrt{(x_f - x_r)^2 + (y_f - y_r)^2 + (z_f - z_r)^2} + |C_{Lf}| + |\sigma_f| \tag{73}$$

where the distance from the desired landing point is evaluated in meters, while the bank angle in degrees. An optimization process is run on the set of initial conditions reported in Table 1. These values are combined in order to create an eight-dimensional set of $5^3 \times 3^5 = 30375$ initial conditions. Then, the two gains n_1, n_2 are optimized employing these initial conditions, using both the *@Particle Swarm Optimization* and the *@fminsearch* routines in Matlab [27]. The output of this optimization process is made up of 30375 pairs of optimal gains n_1, n_2. In the numerical simulations, this set is interpolated (using *@interpn*) in order to obtain the values of the optimal gains also for a generic initial condition.

IV. Nonlinear attitude control

This section is focused on nonlinear attitude control. The attitude control system is designed for the purpose of guaranteeing the correct vehicle orientation, based on the commanded control angles yielded by the guidance scheme.

Table 1 Set of initial conditions

Variable	Values
$x(0)$ [m]	[4000 5000 6000 7000 8000]
$y(0)$ [m]	[-6000 -5000 -4000 -3000 -2000]
$z(0)$ [m]	[6000 7000 8000 9000 10000]
$v_r^G(0)$ [m/s]	[130 170 210]
$\zeta_r^{(G)}(0)$ [deg]	[ζ_f-40 deg $\quad \zeta_f \quad \zeta_f$ + 40 deg]
$\gamma_r^{(G)}(0)$ [deg]	[-40 -10 20]
$C_L(0)$ [-]	[0 0.3 0.6]
$\sigma(0)$ [deg]	[-50 0 50]

As a first step, two kinds of trajectories are distinguished:

- the commanded trajectory, coming from the solution of the translational dynamics $(x, y, z, v_r^{(G)}, \zeta_r^{(G)}, \gamma_r^{(G)})$, together with the two sliding mode equations for the control variables. The commanded trajectory is also termed Guidance Trajectory (GT). For the GT, the kinematics is described using Cartesian variables (x, y, z).
- the actual trajectory (AT), coming from the solution of the translational dynamics $(r, \lambda_g, \varphi, v_r, \zeta_r, \gamma_r)$, together with the attitude dynamics and the feedback relations for the torque (being obtained in this Section).

A. Commanded attitude

The reentry trajectories is divided into sample time intervals $[t_k, t_{k+1}]$. At t_k, the spherical coordinates are used to derive the variables $(x_k, y_k, z_k, v_{rk}^{(G)}, \gamma_{rk}^{(G)}, \zeta_{rk}^{(G)})$, needed as starting conditions for the guidance equations (37) - (42). Then, the the sliding mode control generates the desired trajectory, by identifying the time histories of the lift coefficient and bank angle (while the sideslip angle is nominally set to zero). With the commanded angles α_c and σ_c, the commanded attitude with respect to the II2 frame is identified through the following relationship:

$$\mathbf{R}_{II2\rightarrow C} = \mathbf{R}_A \mathbf{R}_3(-\alpha_c)\mathbf{R}_2(\sigma_c)\mathbf{R}_3(-\beta_W)\mathbf{R}_1(\alpha_W)\mathbf{R}_3(-\gamma_r^{(G)})\mathbf{R}_1(\zeta_r^{(G)})\mathbf{R}_B^T \tag{74}$$

Then, from this matrix, the commanded quaternions are calculated. The wind angles α_W and β_W are updated at the beginning of each sample interval: they are computed from the knowledge of the wind velocity at t_k and kept constant for the entire time interval $[t_k, t_{k+1}]$, in the context of the guidance algorithm.

In order to derive the expression of the commanded torque, the time derivatives of quaternions and angular velocity components are needed. From the fundamental kinematics relationship [25], one obtains

$$\boldsymbol{\omega}_C = 2\left[\frac{q_{0C}^2 \mathbf{I}_{3x3} - q_{0C}\,\tilde{\boldsymbol{q}} + \boldsymbol{q}_C \boldsymbol{q}_C^T}{q_{0C}}\right]^T \dot{\boldsymbol{q}}_C \tag{75}$$

Since both the derivatives of the quaternions and the angular velocity are unknown, the following strategy is applied:

1) obtain the quaternions at 40 discrete times in the sampling interval $[t_k, t_{k+1}]$ from the commanded attitude and use a 3rd degree polynomial to interpolate them;
2) compute the derivatives of the quaternions by analytical derivation of the 3rd-degree polynomial;
3) evaluate the angular velocities by using the fundamental kinematics equation in (75);
4) compute the derivatives of the angular velocity by repeating steps 1) and 2) with the angular velocity components instead of the quaternions.

B. Relative attitude kinematics

The rotation matrix $\underset{B\leftarrow C}{\mathbf{R}}$ that relates the actual body axes (subscript B) to the commanded body axes (subscript C) can be written in terms of the error quaternion $q_0^{(E)}, \boldsymbol{q}^{(E)}$ [28]

$$\underset{B\leftarrow C}{\mathbf{R}} = [q_0^{(E)}]^2 - [\boldsymbol{q}^{(E)}]^T\boldsymbol{q}^{(E)}\mathbf{I}_{3x3} + 2\boldsymbol{q}^{(E)}[\boldsymbol{q}^{(E)}]^T - 2q_0^{(E)}\tilde{\boldsymbol{q}}^{(E)} \tag{76}$$

Moreover, the governing equations for $q_0^{(E)}, \boldsymbol{q}^{(E)}$ are [28]

$$\dot{q}_0^{(E)} = -\frac{1}{2}[\boldsymbol{q}^{(E)}]^T\boldsymbol{\omega}_E \tag{77}$$

$$\dot{\boldsymbol{q}}^{(E)} = \frac{1}{2}q_0^{(E)}\boldsymbol{\omega}_E + \frac{1}{2}\tilde{\boldsymbol{q}}^{(E)}\boldsymbol{\omega}_E \tag{78}$$

where $\boldsymbol{\omega}_E := \boldsymbol{\omega} - \underset{B\leftarrow C}{\mathbf{R}}\boldsymbol{\omega}_C$

C. Feedback law and related stability analysis

The target set for the attitude tracking problem is

$$q_0^{(E)} = 1 \quad \text{and} \quad \boldsymbol{\omega}_E = \mathbf{0} \tag{79}$$

This subsection deals with a feedback control law analogous to that presented in [28]. Its asymptotic stability is proven in the following two propositions.

Proposition 1. *Let* $\mathbf{A}$ *and* $\mathbf{B}$ *denote two constant positive definite matrices;* $\mathbf{A}$ *is also symmetric. The feedback control law*

$$\boldsymbol{T}_c = \tilde{\boldsymbol{\omega}}\mathbf{J}_C^{(B)}\boldsymbol{\omega} - \boldsymbol{M}_c + \mathbf{J}_C^{(B)}[-\tilde{\boldsymbol{\omega}}_E\underset{B\leftarrow C}{\mathbf{R}}\boldsymbol{\omega}_C + \underset{B\leftarrow C}{\mathbf{R}}\dot{\boldsymbol{\omega}}_C] - \mathbf{J}_C^{(B)}\mathbf{A}^{-1}\mathbf{B}\boldsymbol{\omega}_E - \mathbf{J}_C^{(B)}\mathbf{A}^{-1}\boldsymbol{q}^{(E)} \tag{80}$$

drives the system defined by Eqs. (33) and (77) - (78) toward the attracting set associated with $\boldsymbol{\omega}_E = \mathbf{0}$.

Proof. As a first step, the following candidate Lyapunov function is introduced:

$$V = \frac{1}{2}\boldsymbol{\omega}_E^T \mathbf{A}\boldsymbol{\omega}_E + [q_1^{(E)}]^2 + [q_2^{(E)}]^2 + [q_3^{(E)}]^2 + [q_0^{(E)} - 1]^2 = \frac{1}{2}\boldsymbol{\omega}_E^T \mathbf{A}\boldsymbol{\omega}_E + 2(1 - q_0^{(E)}) \tag{81}$$

It is apparent that this function is always positive definite and vanishes only in the target set. Second, V has continuous partial derivatives. Using Eqs. (33) and (77) - (78), the time derivative of V equals

$$\dot{V} = \boldsymbol{\omega}_E^T \mathbf{A}\left\{[\mathbf{J}_C^{(B)}]^{-1}\left(- \tilde{\boldsymbol{\omega}}\mathbf{J}_C^{(B)}\boldsymbol{\omega} + \boldsymbol{M}_c + \boldsymbol{T}_c\right) - \underset{B\leftarrow C}{\dot{\mathbf{R}}}\,\boldsymbol{\omega}_C - \underset{B\leftarrow C}{\mathbf{R}}\,\dot{\boldsymbol{\omega}}_C\right\} + \boldsymbol{\omega}_E^T \boldsymbol{q}^{(E)} \tag{82}$$

Insertion of the feedback law (80) leads to

$$\dot{V} = -\boldsymbol{\omega}_E^T \mathbf{B}\boldsymbol{\omega}_E \tag{83}$$

which is negative (because $\mathbf{B}$ is positive definite), except at $\boldsymbol{\omega}_E = \mathbf{0}$, where $\dot{V}$ vanishes. Definitely, V is a positive definite function, with continuous partial derivatives and such that $\dot{V} < 0$ (unless $\boldsymbol{\omega}_E = \mathbf{0}$), therefore V is a Lyapunov function [29].

Because the attracting set, denoted with A, does not coincide with the target set (79), Proposition 1 does not ensure asymptotic convergence toward the desired final conditions (79). However, the LaSalle's invariance principle can be used to identify the invariant set.

Proposition 2. *The control law (80)drives the dynamical system described by Eqs. (33) and 77 - 78 toward the invariant set associated with* $\boldsymbol{\omega}_E = \mathbf{0}, [q_0^{(E)}]^2 = 1, \boldsymbol{q}^{(E)} = \mathbf{0}$.

Proof. Because $\dot{V}$ is continuous and negative (except at $\boldsymbol{\omega}_E = \mathbf{0}$), the condition $V(q_0^{(E)}(t), \boldsymbol{q}^{(E)}(t), \boldsymbol{q}^{(E)}(t)) \leq V(q_0^{(E)}(t_0), \boldsymbol{q}^{(E)}(t_0), \boldsymbol{q}^{(E)}(t_0))$ defines a compact set C. The invariant set, which plays a crucial role in the LaSalle's principle, is to be sought in $A \cap C$, i.e. in the portion of the attracting set A contained in C. By definition, the invariant set collects all the dynamical states (in the attracting set) that remain unaltered. This means that once the invariant set is reached, $\boldsymbol{\omega}_E = \mathbf{0}$ at future times, which implies $\dot{\boldsymbol{\omega}}_E = \mathbf{0}$, i.e.

$$\dot{\boldsymbol{\omega}}_E = \dot{\boldsymbol{\omega}} - \underset{B\leftarrow C}{\mathbf{R}}\,\dot{\boldsymbol{\omega}}_C + \tilde{\boldsymbol{\omega}}_E \underset{B\leftarrow C}{\mathbf{R}}\,\boldsymbol{\omega}_C = \dot{\boldsymbol{\omega}} - \underset{B\leftarrow C}{\mathbf{R}}\,\dot{\boldsymbol{\omega}}_C = \mathbf{0} \tag{84}$$

Using Eqs. (33) and (79) the preceding relation simplifies to

$$- [\mathbf{J}_C^{(B)}]^{-1}\mathbf{A}\boldsymbol{q}^{(E)} = \mathbf{0} \rightarrow \boldsymbol{q}^{(E)} = \mathbf{0}, [q_0^{(E)}]^2 = 1 \tag{85}$$

This demonstrates that the feedback law (80) drives the system toward the target set.

With this considerations and assuming that the torque disturbance is negligible ($\boldsymbol{M}_c = \mathbf{0}$) the nonlinear feedback

control law is equal to

$$\boldsymbol{T}_c = \tilde{\boldsymbol{\omega}}\mathbf{J}_C^{(B)}\boldsymbol{\omega} + \mathbf{J}_C^{(B)}[-\tilde{\boldsymbol{\omega}}_{\boldsymbol{E}}\underset{B\leftarrow C}{\mathbf{R}}\boldsymbol{\omega}_C + \underset{B\leftarrow C}{\mathbf{R}}\dot{\boldsymbol{\omega}}_C] - \mathbf{J}_C^{(B)}\mathbf{A}^{-1}\mathbf{B}\boldsymbol{\omega}_E - \mathbf{J}_C^{(B)}\mathbf{A}^{-1}\boldsymbol{q}^{(E)} \tag{86}$$

D. Gain selection

The feedback control law (86) is defined in terms of two constant, positive definite matrices, i.e. **A** and **B**. Selection of these matrices affects the transient behavior and the convergence time of the actual attitude toward the commanded one. In this research, these two matrices are selected by assuming that both of them are diagonal and written as

$$\mathbf{A}^{-1} = c_1\mathbf{I}_{3x3} \quad \text{and} \quad \mathbf{B} = c_2\mathbf{I}_{3x3} \tag{87}$$

where c_1 and c_2 are two positive constants.

For the purpose of a preliminary selection of the control gains, in three-axial (full-attitude) maneuvers, the rotation is assumed to occur about the eigenaxis, and the gains of the quaternion-based nonlinear feedback law are found using the second-order equation [28]

$$\ddot{\phi}_E + c_1c_2\dot{\phi}_E + c_1\sin\left(\frac{\phi_E}{2}\right) = 0 \tag{88}$$

where ϕ_E is the principal angle. If ϕ_E is sufficiently small, then $\sin(\phi_E/2) \approx \phi_E/2$, and Eq. (88) assumes the form of a second-order linear differential equation,

$$\ddot{\phi}_E + 2\xi\omega_n\dot{\phi}_E + \omega_n^2\phi_E = 0 \tag{89}$$

with

$$c_1 = 2\omega_n^2 \quad and \quad c_2 = \frac{\xi}{\omega_n} \tag{90}$$

The associated second-order system has damping coefficient ξ and natural frequency ω_n. The selection of these two parameters, which have a straightforward interpretation in relation to the transient behaviour, leads to proper values of c_1 and c_2.

E. Actuation modeling

Torque is actuated through deflection of aerodynamic surfaces (e.g., elevons and body flaps). This control action is described in a simplified way, using a first-order model. This means that the actual torque $\boldsymbol{T}_a$ is governed by the following first-order differential equation:

$$\dot{\boldsymbol{T}}_a = \frac{\boldsymbol{T}_c - \boldsymbol{T}_a}{\tau} \tag{91}$$

where $\boldsymbol{T}_c$ is given by Eq. (86) and the time constant τ is set to 0.5 s. Moreover, torque saturation is modeled as well, by assuming that each torque component has a maximum magnitude of 10^6 Nm (this upper bound is an order of magnitude less than [26]).

F. Actual attitude

The attitude matrix can be expressed in terms of quaternions [25] as

$$\mathbf{R}_{II2\to B} = (q_0^2 - \boldsymbol{q}^T\boldsymbol{q})\mathbf{I}_{3x3} + 2\boldsymbol{q}\boldsymbol{q}^T - 2q_0\tilde{\boldsymbol{q}} \tag{92}$$

Matrix $\mathbf{R}_{\alpha\beta\sigma}$ is defined as

$$\mathbf{R}_{\alpha\beta\sigma} = \mathbf{R}_1(\beta)\mathbf{R}_3(-\alpha)\mathbf{R}_2(\sigma) \tag{93}$$

Following the sequence of the rotation matrices

$$\mathbf{R}_{\alpha\beta\sigma} = \mathbf{R}_A^T\mathbf{R}_{II2\to B}\left[\mathbf{R}_3(-\beta_w)\mathbf{R}_1(\alpha_w)\mathbf{R}_3(-\gamma_r)\mathbf{R}_1(\zeta_r)\mathbf{R}_2(-\varphi)\mathbf{R}_3(\lambda_g)\mathbf{R}_3(\theta_G)\mathbf{R}_3(\lambda_k)\mathbf{R}_2(-\varphi_k)\mathbf{R}_B^T\right]^T \tag{94}$$

From comparison of Eqs. (93) and (94), one can find the actual aerodynamics angles, in terms of known quantities,

$$\alpha = -\text{atan2}\left[\mathbf{R}_{\alpha\beta\sigma}(1,2), \mathbf{R}_{\alpha\beta\sigma}(2,2)\right] \tag{95}$$

$$\sigma = \text{atan2}\left[\mathbf{R}_{\alpha\beta\sigma}(3,1), \mathbf{R}_{\alpha\beta\sigma}(3,3)\right] \tag{96}$$

$$\beta = \arcsin\left[\mathbf{R}_{\alpha\beta\sigma}(3,2)\right] \tag{97}$$

where $\mathbf{R}_{\alpha\beta\sigma}(i,j)$ is the entry in the i-th row and j-th column of $\mathbf{R}_{\alpha\beta\sigma}$. Once these angles are computed, the state variables are updated by numerical integration: the actual attitude must pursue the commanded attitude and the actual aerodynamics angles determine the actual trajectory. After computing the actual trajectory, the algorithm proceeds to the next sampling interval $[t_{k+1}, t_{k+2}]$.

The diagram in Figure 2 summarizes the algorithm. The complete system for the AT generation is made up of the

set of 16 differential equations (27)-(32), (34)-(35), (33), and (91).

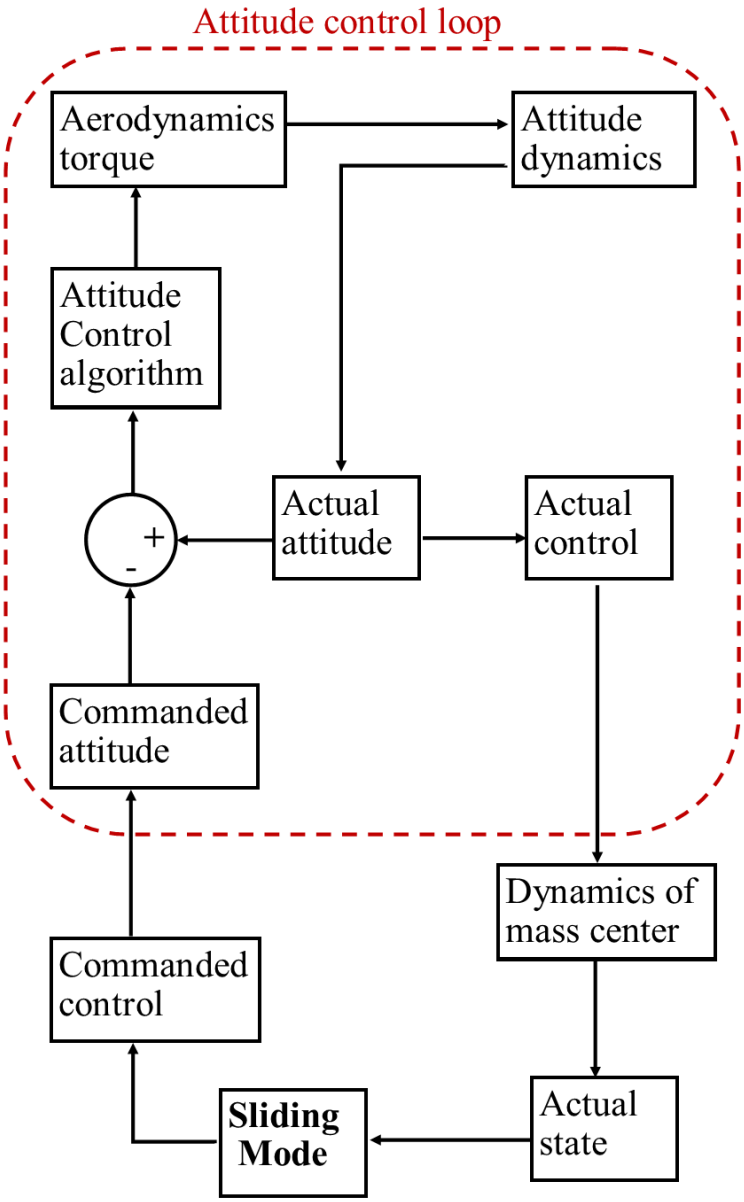

Fig. 2 Guidance and Control algorithm

V. Numerical simulations

The methodology based on the joint use of sliding mode guidance and nonlinear attitude control is tested by means of a Monte Carlo campaign.

A. Simulation setup

Table 2 collects the set of initial conditions and standard deviations, assuming a Gaussian distribution. $(\tilde{x}, \tilde{y}, \tilde{z})$ indicates the set of cartesian coordinates in the AL frame. In order to consider the atmospheric density variation in the model, a displacement is introduced, so the atmosphere density in Eqs. (27)-(32) becomes

$$\rho = \rho_0 \exp\left(-z/H\right)(1 + \Delta_{rho}) \tag{98}$$

where Δ_{rho} is the random uncertain value, with uniform distribution in [-0.02,+0.02].

Table 2 Initial conditions and standard deviations

Variable	Initial Condition	Standard Deviation
$\tilde{x}(0)$ [m]	6000	500
$\tilde{y}(0)$ [m]	-4000	500
$\tilde{z}(0)$ [m]	8000	500
$v_r^{(G)}(0)$ [m/s]	170	10
$\zeta_r^{(G)}(0)$ [deg]	ζ_f	10
$\gamma_r^{(G)}(0)$ [deg]	-10	8
$\alpha(0)$ [deg]	20	3
$\sigma(0)$ [deg]	0	10
$\omega_x(0)$ [deg]	0	5
$\omega_y(0)$ [deg]	0	5
$\omega_z(0)$ [deg]	0	5
u_{xy} [m/s]	0	3

A total number of 500 simulations are run and the initial conditions are randomly generated with an upper/lower bounds set to $\pm 2\sigma_s$ (where σ_s denotes the standard deviation of the variable of interest and the bounds represent reasonable physical limits, introduced to avoid the stochastic generation of unrealistic initial conditions in the Monte Carlo campaign). Each sampling interval has a duration of 1 s, while the gains of the nonlinear control law are tuned to achieve a good performance and simultaneously satisfy the limits on the torque,

$$\omega_n = 5 \ \text{rad/s} \qquad \xi = 5 \tag{99}$$

B. Numerical results

The downrange and crossrange components (r_{down}, r_{cross}) allow to understand the position of the vehicle along the landing runway. These are directly calculated from the ALI frame components through an elementary rotation along axis 1.

$$r_{down} = \begin{bmatrix} x & y & z \end{bmatrix} \mathbf{R}_1^T(\zeta_{rwy}) \begin{bmatrix} 0 & 1 & 0 \end{bmatrix}^T \tag{100}$$

$$r_{cross} = \begin{bmatrix} x & y & z \end{bmatrix} \mathbf{R}_1^T(\zeta_{rwy}) \begin{bmatrix} 0 & 0 & 1 \end{bmatrix}^T \tag{101}$$

Table 3 collects the statistics on the simulations, i.e. the final conditions that occur at touchdown, when the altitude of the center of mass reduces to 3 m. From inspection of Table 3, it is evident the capability of the algorithm to guide the vehicle despite the wind and the deviations on the initial conditions. In fact, the standard deviation on the downrange component is modest with respect to the runway length, while the crossrange component is negligible. The mean value of the heading angle is close to the nominal runway direction ζ_{rwy}, also, the mean value of the radial velocity is close to $\dot{h}_{des}$, and the respective standard deviation is still within the safety limits of the landing gear, which is set to -3 m/s [18]. From inspection of the aerodynamics angles it is apparent that the sideslip angle remains close to 0, while the bank angle tends to 0 while approaching the runway, for all cases.

Table 3 Results of the Monte Carlo campaign

Variable	Mean	Standard Deviation
Downrange [m]	1.69	9.65
Crossrange [m]	$-6.96 \cdot 10^{-3}$	0.12
Radial velocity [m/s]	-1.31	0.39
Heading angle [deg]	-60.23	$7.6 \cdot 10^{-3}$
Flight path angle [deg]	-0.75	0.25
Attack angle [deg]	22.95	2.11
Bank angle [deg]	0.15	0.05
Sideslip angle [deg]	-0.14	0.12

Figure 3 shows the stream of trajectories leading toward a smooth landing on the runway. From Figure 5, it is clear that the algorithm is able to reduce the radial velocity up to the desired landing rate. Figure 6 highlights the successful alignment with the runway despite the significant error on the initial heading angle. Figures 8 and 9 show the time histories of the aerodynamic angles. The control inputs generated by the guidance algorithm, i.e. bank angle and angle of attack, are saturated so that only feasible trajectories are generated. Figure 10 highlights an important difference between the guidance trajectory and the actual trajectory. Although the guidance algorithm generates trajectories with $\beta = 0$, along the actual trajectory the sideslip angle is induced by the tracking error between the commanded and the actual attitude. Moreover, it is increased by the wind. Nevertheless, the system is capable of driving the sideslip angle close to the nominal value, i.e. 0, with modest final values. Figure 4 shows the scalar component of the error quaternion converging to 1, and the vector components converging to 0, meaning that the tracking law forces the attitude toward the commanded attitude. Figures 11 through 13 are the time histories of the actual angular velocity components. The saturation of the commanded torque and the conditions in the equations 70 - 72 keep their values within the allowed range. The x and z components of the angular velocity converge to zero, while the y component converges to modest

negative values, due to oscillations on the pitch torque during the flare phase shortly before touchdown.

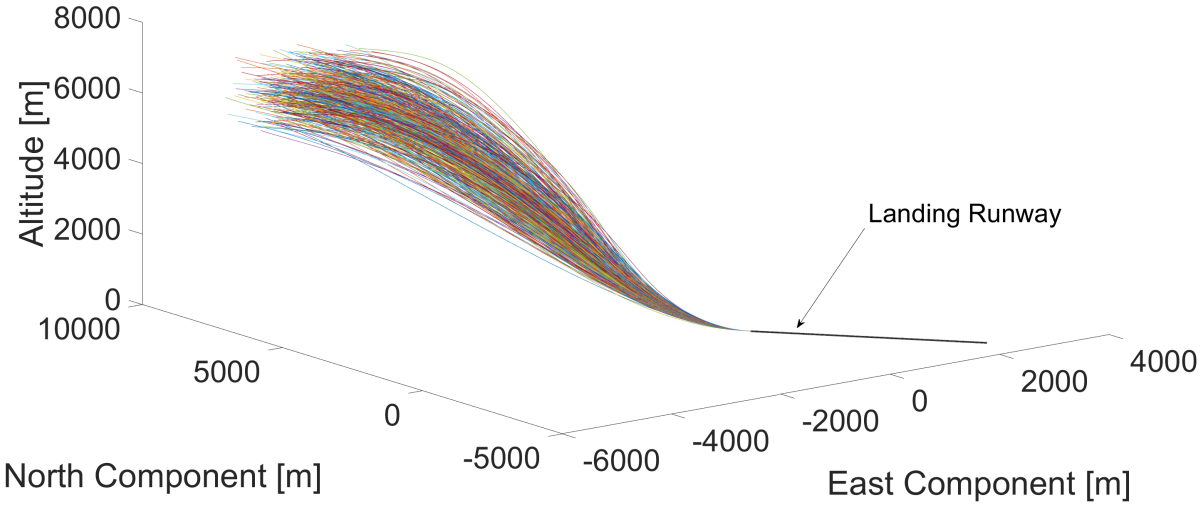

Fig. 3 Trajectory

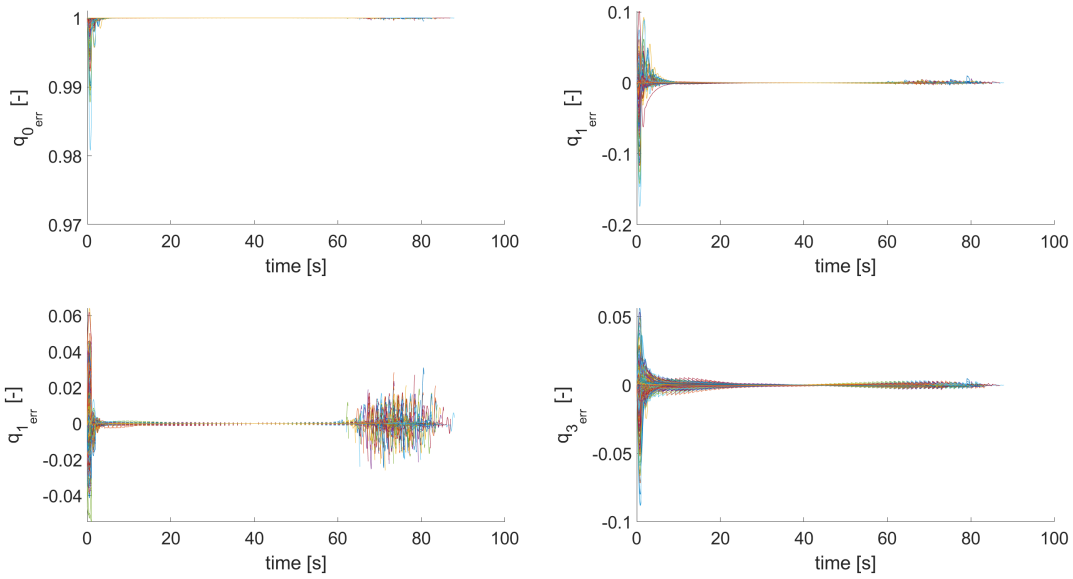

Fig. 4 Error quaternion

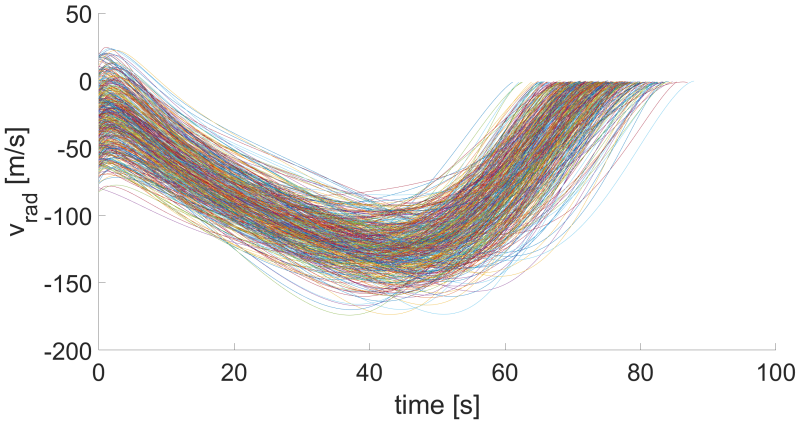

Fig. 5 Radial velocity

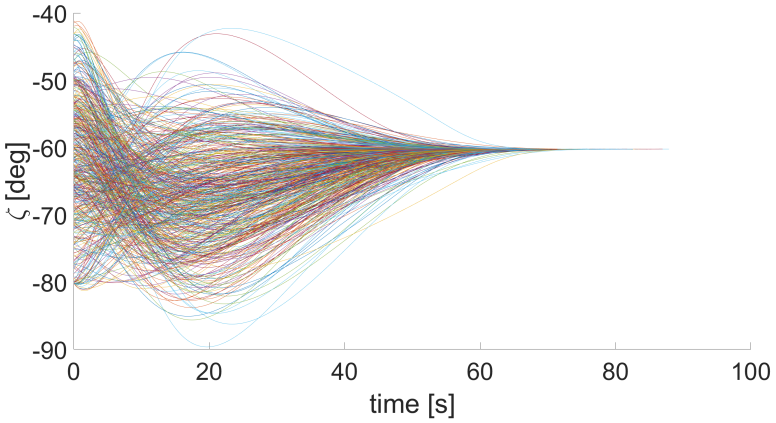

Fig. 6 Heading Angle

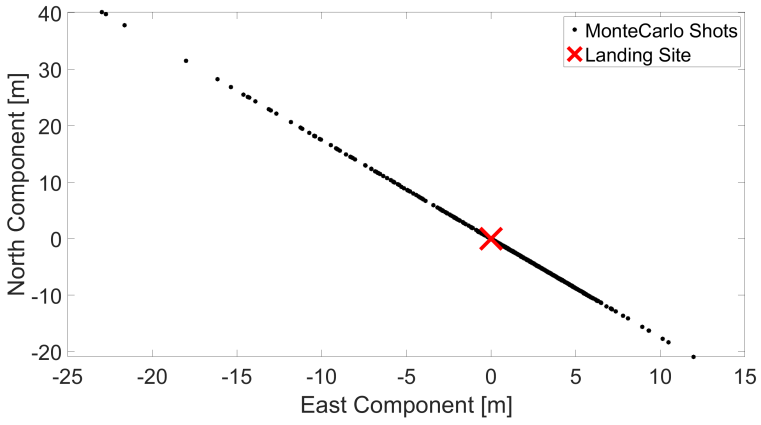

Fig. 7 Distribution of final position with respect to the nominal landing site

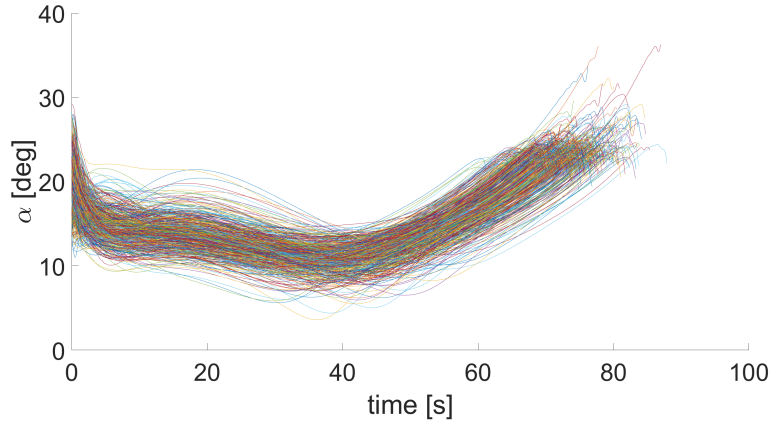

Fig. 8 Attack Angle

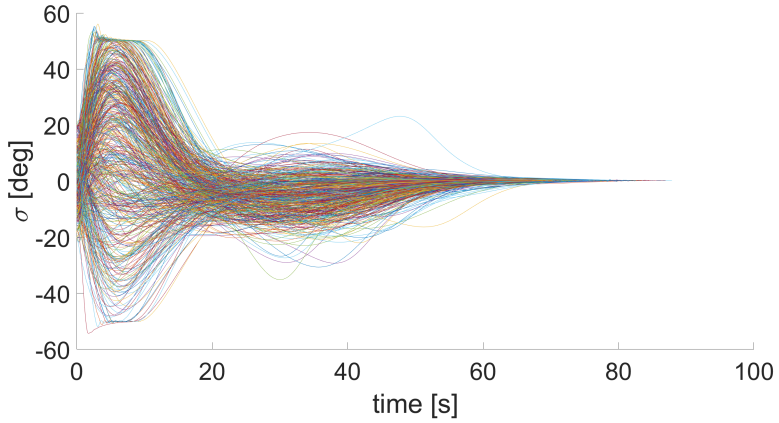

Fig. 9 Bank Angle

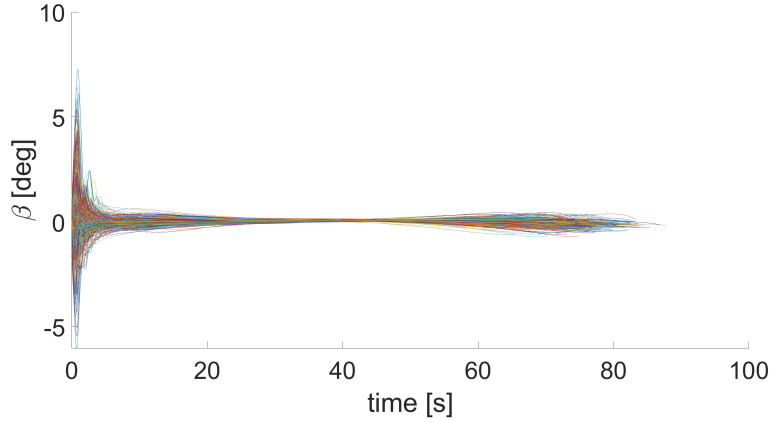

Fig. 10 Sideslip Angle

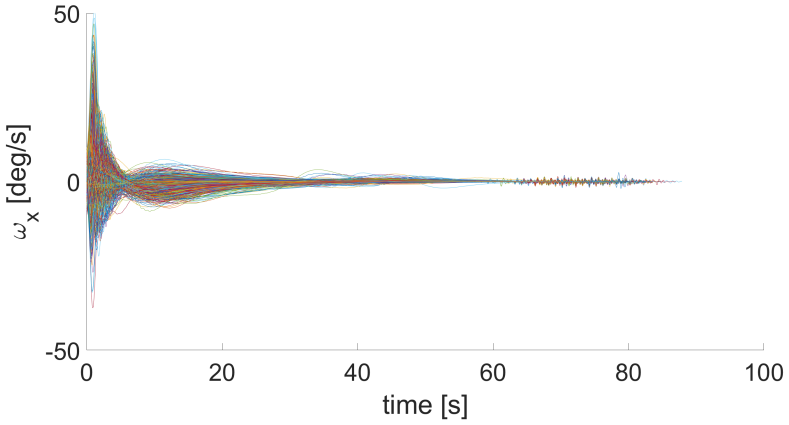

Fig. 11 Angular Velocity (X-component)

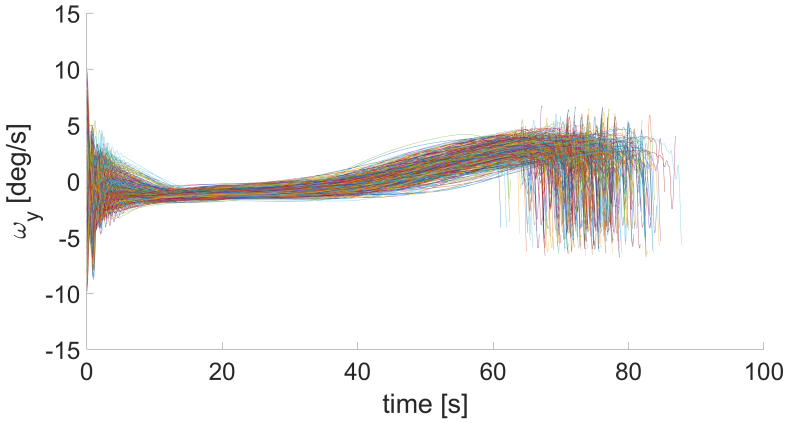

Fig. 12 Angular Velocity (Y-component)

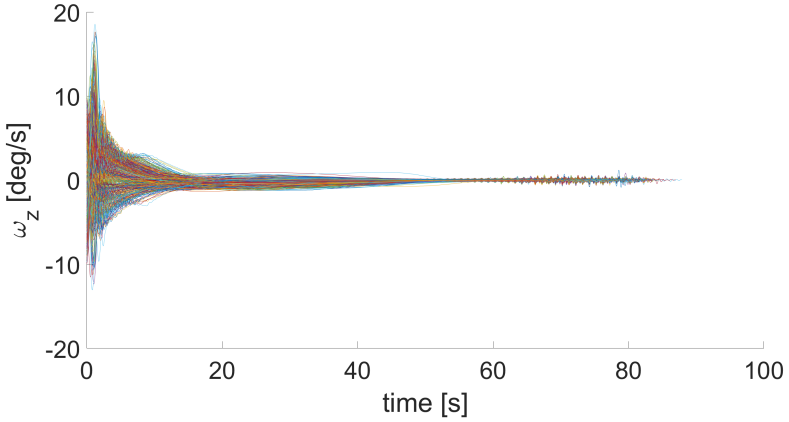

Fig. 13 Angular Velocity (Z-component)

VI. Concluding remarks

This research introduces and describes a new guidance and control architecture for autonomous descent and landing of an unpowered lifting vehicle. More specifically, the reentry vehicle is driven toward a specified landing point, with prescribed values of the vertical velocity and heading angle, for correct alignment with the runway. The real-time guidance strategy is based on multiple sliding surfaces. The first surface is responsible for driving the vehicle to the landing site with the final desired vertical velocity, while the second sliding surface guarantees the convergence toward the desired landing point, with the appropriate heading angle, aligned with the runway. The time derivatives of the lift coefficient and bank angle are used as control inputs, whereas the definition of the sliding surfaces is such that these two inputs are involved simultaneously in the lateral and the vertical guidance. These two control variables are constrained to suitable intervals for practical feasibility, so that only realistic trajectories can be generated by the guidance algorithm. Moreover, a new approach is proposed that allows selecting the convergence rate toward the sliding surfaces. This methodology is based on adaptive coefficients and is useful for the proper tuning of the control effort, according to the instantaneous size of the sliding surface, thus circumventing potential numerical difficulties. Moreover, this study addresses the heuristic optimization of the guidance gains, over a large set of initial conditions. Quaternion-based nonlinear attitude control, enjoying quasi-global stability properties, is used to drive the actual attitude toward the commanded one, which is provided by the guidance algorithm. Effectiveness and accuracy of the guidance and control strategy at hand is tested by means of a Monte Carlo campaign, in the presence of stochastic wind and large dispersion on the initial conditions. The results coming from these numerical simulations unequivocally demonstrate that the guidance and control strategy at hand is able to drive the lifting vehicle to safe landing, even in challenging scenarios, while guaranteeing a modest vertical velocity at touchdown, the correct heading angle, and a limited distance from the desired landing point. This research adopts simplified modeling of the actual torque needed to perform attitude maneuvering. In more advanced phases of design and implementation of the guidance and control architecture at hand, the actual torque components are to be modeled in relation to the deflections of lifting surfaces used for aerodynamics control.

VII. Appendix

This appendix shows the computation of the sliding mode guidance coefficients $a_1, a_2, b_1, b_2, c_{11}, c_{21}, c_{12}, c_{22}$, in Eq. (51). In order to do so, the second and third derivatives of the sliding surface s_1 must be calculated. It is assumed that the time derivatives of the wind angles and velocity components are negligible,

$$\dot{v}_{w,1} \approx \dot{v}_{w,2} \approx \dot{v}_{w,3} \approx \dot{\alpha}_W \approx \dot{\beta}_W \approx 0 \tag{102}$$

The time derivative of the vehicle velocity with respect to the atmosphere is

$$\dot{v}_W = \frac{(v_r^{(G)} - v_{w,2})\dot{v}_r^{(G)}}{v_W} \tag{103}$$

Then, the time derivative of the density of the atmosphere is computed as

$$\dot{\rho} = \frac{\dot{x}}{H}\rho \tag{104}$$

The partial derivative of the rotation matrix $\mathbf{R}_2(\sigma)$ with respect to σ is

$$\frac{\partial \mathbf{R}_2(\sigma)}{\partial \sigma} = \begin{bmatrix} -\sin\sigma & 0 & -\cos\sigma \\ 0 & 0 & 0 \\ \cos\sigma & 0 & -\sin\sigma \end{bmatrix} \tag{105}$$

Then, for the sake of simplicity, the following vectors and matrices are defined:

$$\boldsymbol{u}_x = \begin{bmatrix} 1 & 0 & 0 \end{bmatrix}^T \qquad \boldsymbol{u}_y = \begin{bmatrix} 0 & 1 & 0 \end{bmatrix}^T \qquad \boldsymbol{u}_z = \begin{bmatrix} 0 & 0 & 1 \end{bmatrix}^T \tag{106}$$

$$\tilde{\mathbf{R}} = \frac{\partial \mathbf{R}_2(\sigma)}{\partial \sigma}\mathbf{R}_3(\beta_W)\mathbf{R}_1(\alpha_W) \tag{107}$$

$$\boldsymbol{\delta}^T = \frac{S_{ref}}{m}\begin{bmatrix} C_L\left(\rho v_W \dot{v}_W + \frac{1}{2}\rho v_W^2\right) & -C_D\left(\rho v_W \dot{v}_W + \frac{1}{2}\rho v_W^2\right) & 0 \end{bmatrix}\tilde{\mathbf{R}} \tag{108}$$

$$\boldsymbol{\epsilon}^T = \frac{S_{ref}}{m}\begin{bmatrix} \frac{1}{2}\rho v_W^2 & -KC_L\rho v_W^2 & 0 \end{bmatrix}\tilde{\mathbf{R}} \tag{109}$$

$$\boldsymbol{\iota}^T = \frac{S_{ref}}{m}\begin{bmatrix} L & -D & 0 \end{bmatrix}\mathbf{R}_2(\sigma)\mathbf{R}_3(\beta_W)\mathbf{R}_1(\alpha_W) \tag{110}$$

Finally, the full expression of the coefficients $a_1, a_2, b_1, b_2, c_{11}, c_{21}, c_{12}, c_{22}$, is reported

$$a_1 = \dot{v}_r^{(G)}\sin\gamma_r^{(G)} + \dot{\gamma}_r^{(G)} v_r^{(G)}\cos\gamma_r^{(G)} \tag{111}$$

$$a_2 = \dot{v}_r^{(G)}\left(\cos\gamma_r^{(G)}\sin\zeta_r^{(G)} - \cos\gamma_r^{(G)}\cos\zeta_r^{(G)}\tan\zeta_{rwy}\right)+ \dot{\gamma}_r^{(G)}\left(-v_r^{(G)}\sin\gamma_r^{(G)}\sin\zeta_r^{(G)} + v_r^{(G)}\sin\gamma_r^{(G)}\cos\zeta_r^{(G)}\tan\zeta_{rwy}\right)+ \dot{\zeta}_r^{(G)}\left(-v_r^{(G)}\cos\gamma_r^{(G)}\sin\zeta_r^{(G)} + v_r^{(G)}\cos\gamma_r^{(G)}\sin\zeta_r^{(G)}\tan\zeta_{rwy}\right) \tag{112}$$

$$b_1 = \boldsymbol{\delta}^T\left(\sin\gamma_r^{(G)}\boldsymbol{u}_y + \cos\gamma_r^{(G)}\boldsymbol{u}_x\right) + \dot{\gamma}_r^{(G)}\left(A_v\cos\gamma_r^{(G)} - A_n\sin\gamma_r^{(G)}\right) \tag{113}$$

$$b_2 = \left(\cos\zeta_r^{(G)} + \sin\zeta_r^{(G)}\tan\zeta_{rwy}\right)\left(\boldsymbol{\delta}^T\boldsymbol{u}_z + A_v\dot{\zeta}_r^{(G)}\cos\gamma_r^{(G)} - A_n\dot{\zeta}_r\sin\gamma_r^{(G)}\right) + \left(\sin\zeta_r^{(G)} - \cos\zeta_r^{(G)}\tan\zeta_{rwy}\right)+ \left[\boldsymbol{\delta}^T\left(\cos\gamma_r^{(G)}\boldsymbol{u}_y - \sin\gamma_r^{(G)}\boldsymbol{u}_x\right) - A_v\dot{\gamma}_r^{(G)}\sin\gamma_r^{(G)} - A_n\dot{\gamma}_r^{(G)}\cos\gamma_r^{(G)} - A_h\dot{\zeta}_r^{(G)}\right] \tag{114}$$

$$c_{11} = \boldsymbol{\epsilon}^T\left(\boldsymbol{u}_y\sin\gamma_r^{(G)} + \boldsymbol{u}_x\cos\gamma_r^{(G)}\right) \tag{115}$$

$$c_{12} = \boldsymbol{\iota}^T\left(\boldsymbol{u}_y\sin\gamma_r^{(G)} + \boldsymbol{u}_x\cos\gamma_r^{(G)}\right) \tag{116}$$

$$c_{21} = \boldsymbol{\epsilon}^T\left(\sin\zeta_r^{(G)} - \cos\gamma_r^{(G)}\tan\zeta_{rwy}\cos\gamma_r^{(G)}\boldsymbol{u}_y - \sin\gamma_r^{(G)}\boldsymbol{u}_x\right) + \boldsymbol{u}_z(\cos\zeta_r^{(G)} + \sin\zeta_r^{(G)}\tan\zeta_{rwy}) \tag{117}$$

$$c_{21} = \boldsymbol{\iota}^T\left(\sin\zeta_r^{(G)} - \cos\gamma_r^{(G)}\tan\zeta_{rwy}\cos\gamma_r^{(G)}\boldsymbol{u}_y - \sin\gamma_r^{(G)}\boldsymbol{u}_x\right) + \boldsymbol{u}_z(\cos\zeta_r^{(G)} + \sin\zeta_r^{(G)}\tan\zeta_{rwy}) \tag{118}$$

References

[1] Chapman, D. R., *An approximate analytical method for studying entry into planetary atmospheres*, US Government Printing Office, 1959.

[2] Frostic, F., and Vinh, N. X., "Optimal Aerodynamic Control by Matched Asymptotic Expansions," *Acta Astronautica*, Vol. 3, 1976, pp. 319–332. https://doi.org/10.1016/0094-5765(76)90139-9.

[3] Vinh, N. X., *Optimal Trajectories in Atmospheric Flight*, 1st ed., Elsevier, New York, 1981, pp. 296–313.

[4] Broglio, L., "A General Theory on Space and Re-Entry Similar Trajectories," *AIAA Journal*, Vol. 2, No. 10, 1964, p. 1774–1781. https://doi.org/10.2514/3.2664.

[5] Kluever, C. A., *Space Flight Dynamics*, 2nd ed., Wiley, Chichester, 2018, pp. 418–422.

[6] Haya, R., Castellani, L. T., and Ayuso, A., "Re-Entry GNC Concept For A Reusable Orbital Platform (Space Rider)," *69th International Astronautical Congress, Bremen, Germany, IAC-18 D*, Vol. 2, 2018, p. 5.

[7] Sagliano, M., Trigo, G. F., and Schwarz, R., "Preliminary guidance and navigation design for the upcoming DLR reusability flight experiment (ReFEx)," 2018.

[8] Krevor, Z., Howard, R., Mosher, T., and Scott, K., "Dream chaser commercial crewed spacecraft overview," *17th AIAA International Space Planes and Hypersonic Systems and Technologies Conference*, 2011, p. 2245. https://doi.org/10.2514/6.2011-2245.

[9] Bihari, B., Tigges, M., Stephens, J.-P., Vos, G., Bilimoria, K., Mueller, E., Law, H., Johnson, W., Bailey, R., and Jackson, B., "Orion capsule handling qualities for atmospheric entry," *AIAA Guidance, Navigation, and Control Conference*, 2011, p. 6264. https://doi.org/10.2514/6.2011-6264.

[10] D.Mease, K., and Kremer, J.-P., "Shuttle Entry Guidance Revisited Using Nonlinear Geometric Methods," *Journal of Guidance, Control, and Dynamics*, Vol. 17, No. 6, 1994, pp. 1350–1356. https://doi.org/10.2514/3.21355.

[11] Benito, J., and Mease, K. D., "Nonlinear Predictive Controller for Drag Tracking in Entry Guidance," *AIAA/AAS Astrodynamics Specialist Conference and Exhibit*, Honolulu, Hi, 2008. https://doi.org/10.2514/6.2008-7350.

[12] Minwen, G., and Dayi, W., "Guidance Law for Low-Lift Skip Reentry Subject to Control Saturation Based on Nonlinear Predictive Control," *Aerospace Science and Technology*, Vol. 37, No. 6, 2014, pp. 48–54. https://doi.org/10.1016/j.ast.2014.05.004.

[13] Lu, P., "Entry Guidance: A Unified Method," *Journal of Guidance, Control, and Dynamics*, Vol. 37, No. 3, 2014, pp. 713–728. https://doi.org/10.2514/1.62605.

[14] Kluever, C. A., "Unpowered Approach and Landing Guidance Using Trajectory Planning," *Journal of Guidance, Control, and Dynamics*, Vol. 27, No. 6, 2004, pp. 967–974. https://doi.org/10.2514/1.7877.

[15] Bollino, M. R. K., and Doman, D., *Optimal Nonlinear Feedback Guidance for Reentry Vehicles*, AIAA Paper 2006-6074, 2006. https://doi.org/10.2514/6.2006-6074.

[16] Fahroo, F., and Doman, D., *A Direct Method for Approach and Landing Trajectory Reshaping with Failure Effect Estimation*, AIAA Paper 2004-4772, 2004. https://doi.org/10.2514/6.2004-4772.

[17] Liu, X., Zhang, F., Li, Z., and Zhao, Y., "Approach and Landing Guidance Design for Reusable Launch Vehicle Using Multiple Sliding Surfaces Technique," *Chinese Journal of Aeronautics*, Vol. 30, No. 4, 2017, pp. 1582–1591. https://doi.org/10.1016/j.cja.2017.06.008.

[18] Harl, N., and Balakrishnan, S. N., "Reentry Terminal Guidance Through Sliding Mode Control," *Journal of Guidance, Control, and Dynamics*, Vol. 33, No. 1, 2010, pp. 186–199. https://doi.org/10.2514/1.42654.

[19] Vitiello, A., Leonardi, E. M., and Pontani, M., "Multiple-sliding-surface guidance and control for terminal atmospheric reentry and precise landing," *IAC 72nd International Astronautical Congress*, Dubai, UAE, 2021.

[20] Virgili, J., Roberts, P. C., and Hara, N. C., "Atmospheric interface reentry point targeting using aerodynamic drag control," *Journal of Guidance, Control, and Dynamics*, Vol. 38, No. 3, 2015, pp. 403–413. https://doi.org/10.2514/1.G000884.

[21] Fedele, A., Omar, S., Cantoni, S., Savino, R., and Bevilacqua, R., "Precise re-entry and landing of propellantless spacecraft," *Advances in Space Research*, Vol. 68, No. 11, 2021, pp. 4336–4358. https://doi.org/10.1016/j.asr.2021.09.029.

[22] Fedele, A., Carannante, S., Grassi, M., and Savino, R., "Aerodynamic control system for a deployable re-entry capsule," *Acta Astronautica*, Vol. 181, 2021, pp. 707–716. https://doi.org/10.1016/j.actaastro.2020.05.049.

[23] *Flying qualities of piloted airplanes*, U.S. Military Specification MIL-F-8785C, 5 November, 1980, pp. 45–60.

[24] Weiland, C., *Aerodynamic Data of Space Vehicles*, Springer-Verlag, Berlin, 2014, pp. 174–197. https://doi.org/10.1007/978-3-642-54168-1.

[25] Hughes, P. C., *Spacecraft Attitude Dynamics*, 2nd ed., Dover Publications Inc., Mineola, 2004, pp. 6–38.

[26] Tian, B., Cui, J., Lu, H., and Zong, H., "Reentry Attitude Control for RLV Based on Adaptive Event-Triggered Sliding Mode," *IEEE Access*, Vol. 7, 2019, pp. 68429– 68435. https://doi.org/10.1109/ACCESS.2019.2917888.

[27] Bober, W., *Numerical and Analytical Methods with Matlab for Engineers and Scientists*, New York: CRC Press, 2013. https://doi.org/10.1201/b16030.

[28] Weiss, H., "Quaternion-Based Rate/Attitude Tracking System with Application to Gimbal Attitude Control," *Journal of Guidance, Control, and Dynamics*, Vol. 16, No. 4, 1993, pp. 609–616. https://doi.org/10.2514/3.21057.

[29] Sastry, S., *Nonlinear Systems. Analysis, Stability, and Control*, Springer, New York, NY, 1999, pp. 384–423. https://doi.org/10.1007/978-1-4757-3108-8.